

# Effects of Size Reduction on the Electrical Transport Properties of 3D Bi Nanowire Networks

Michael Florian Peter Wagner,\* Anna Sarina Paulus, Joachim Brötz, Wilfried Sigle, Christina Trautmann, Kay-Obbe Voss, Friedemann Völklein, and Maria Eugenia Toimil-Molares\*

3D nanowire networks are fascinating systems for future microelectronic devices. They can be handled like macroscopic objects, while exhibiting properties of nanoscale materials. Here, the fabrication of free-standing 3D bismuth nanowire networks with well-controlled and systematically adjusted wire diameter and interconnectivity is presented. The samples are fabricated by pulse electroplating of bismuth into the pores of ion track-etched membranes using an aqueous electrolyte. By optimizing the growth parameters, homogeneously grown, mechanically self-supporting and free-standing networks without a supporting matrix are achieved. Cross-plane Seebeck coefficient and electrical resistance values are investigated as a function of nanowire diameter and temperature. The unique characteristics of these highly interconnected and mechanically self-supported Bi 3D nanowire networks offer exciting perspectives for their implementation in, e.g., infrared detection based on thermoelectric effects, sensing, and THz applications.

## 1. Introduction

Nanowire networks (NWNs) consist of macroscopic areas of highly interconnected nanowires. Due to their adjustable size (up to several cm<sup>2</sup>) they can be easily handled and integrated in larger set-ups and devices. Compared to the standard arrays of parallel nanowires, the numerous junctions between adjacent nanowires in an interconnected network renders mechanical stability (see Figure S1 in the Supporting Information) and higher electrical reliability.<sup>[1–3,5]</sup> These characteristics are of special interest for numerous emerging applications such as thermoelectric sensing, transparent conductors, or selective catalysis for green fuels.<sup>[1,3,6–12]</sup>


For nanowires of lateral dimension comparable to the mean free path of the carriers, the electrical transport is influenced by finite size effects.<sup>[13–23]</sup> For example, the temperature dependence of the electrical resistance in low dimensional systems is less affected by temperature, as the electrical resistance is dominated by scattering effects of the charge carriers with the surface. Descriptions of the scattering of charge carriers on grain boundaries were done by Mayadas and Shatzkes and the models of Fuchs-Sondheimer and Dingle describe the scattering on surfaces.<sup>[24–28]</sup> Quantum size effects, on the other hand, are exhibited when the object size is in the order of the charge carrier Fermi wavelength. Due to the low dimensionality of the quantum wires the electronic density of states significantly differs from the bulk material, which in turn impacts on the transport properties.<sup>[14,29,30]</sup> In the case of 3D nanowire networks, carrier transport can be at the same time influenced by additional scattering effects at the intersections between adjacent nanowires, which number can be systematically adjusted by varying nanowire density and/or size.<sup>[31,32]</sup> In this way, the morphology of the sample can be customized from a network of interconnected individual nanowires whose transport is dominated by the individual nanowire properties to a porous film with bulk-like transport properties. Due to the experimental difficulty to fabricate NWNs with controlled hierarchical assembly and geometry, experimental data on the influence of wire interconnects on the transport properties are still scarce.<sup>[4,8,33,34]</sup>

Dr. M. F. P. Wagner, A. S. Paulus, Prof. C. Trautmann, Dr. K.-O. Voss, Dr. M. E. Toimil-Molares  
 Materials Research Department  
 GSI Helmholtz Center  
 Planckstr. 1, Darmstadt 64291, Germany  
 E-mail: F.M.Wagner@gsi.de; M.E.ToimilMolares@gsi.de

Dr. J. Brötz  
 Department of Materials and Earth Sciences  
 Technische Universität Darmstadt  
 Alarich-Weiss-Straße 2, Darmstadt 64287, Germany

Dr. W. Sigle  
 Max Planck Institute for Solid State Research  
 Heisenbergstraße 1, Stuttgart 70569, Germany

Prof. F. Völklein  
 Institute of Microtechnologies  
 RheinMain University of Applied Sciences  
 Am Brückweg 26, Rüsselsheim 65428, Germany

 The ORCID identification number(s) for the author(s) of this article can be found under <https://doi.org/10.1002/aelm.202001069>.

© 2021 The Authors. Advanced Electronic Materials published by Wiley-VCH GmbH. This is an open access article under the terms of the Creative Commons Attribution License, which permits use, distribution and reproduction in any medium, provided the original work is properly cited.

DOI: 10.1002/aelm.202001069

With regards to transport properties of low dimensional materials the semimetal bismuth is especially interesting. Its highly anisotropic Fermi surface leads to low carrier concentrations, small effective mass, long mean free path ( $\approx 100$  nm at room temperature and as large as  $400 \mu\text{m}$  at  $4.2$  K) and a large Fermi wavelength ( $\approx 40$  nm at room temperature) of the charge carriers.<sup>[13,14,35–37]</sup> This allows the study of finite size effects and quantum confinement already at relatively large nanowire diameters.<sup>[64,65]</sup> Additionally, size reduction leads to a shift in band energies, leading to a semimetal-to-semiconductor transition. Critical diameters for this transition in cylindrical wires were calculated to be at around  $40$ – $55$  nm at  $77$  K, depending on the crystal orientation.<sup>[38,39]</sup> The transition is also interesting for thermoelectric and topological insulator applications, as the effect might be used to generate larger Seebeck coefficients in very thin wires when compared to bulk material.<sup>[13,30,35,40]</sup>

Bismuth nanowires can be prepared by several methods including hydro- and solvothermal synthesis, stress-induced growth, vapor liquid solid methods, the Taylor process and the so-called template method.<sup>[1–3,35,40–51]</sup> The template method, applied in this work, is based on the deposition of material into nanochannels of a given matrix. Thus, wire diameter, density number and alignment are determined by the properties of the hosting membrane.

As templates usually porous anodic alumina oxide or ion track-etched polymer membranes are applied. Martín-González et al. reported the synthesis of  $\text{Bi}_2\text{Te}_3$  nanowire networks by electrodeposition in porous alumina.<sup>[52]</sup> However, alumina is usually removed in alkaline solutions, which causes oxidation of the electrodeposited nanostructures.

The NWNWs characterized in this work were fabricated by pulsed electrodeposition in etched ion-track polycarbonate membranes. The fabrication of the etched ion-track membranes involves two separate processing steps: i) Sequential irradiation of a polymer film from various directions with swift heavy ions; each individual ion creates a damage trail, the so-called ion track.<sup>[53]</sup> ii) Converting the ion tracks into open channels by selective chemical etching, leading to the formation of an interconnected channel system.<sup>[1–3,8]</sup>

Nanochannel density and spatial orientation as well as diameter and geometry are adjusted by the irradiation and etching conditions, respectively. An advantage of polymer membranes is their much lower thermal conductivity ( $\approx 0.21 \text{ W m}^{-1} \text{ K}^{-1}$  at room temperature) compared to porous alumina.<sup>[54]</sup> This allows the measurement of the Seebeck coefficient of the NWNWs within the template, without introducing a large error due to thermal bypasses. Furthermore, the polycarbonate (PC) templates are resistant to electrolytes ranging from strong acidic to alkaline solutions, but can also be easily dissolved in organic solvents without damaging the wires. The application of pulsed plating for the growth process then allows a more homogeneous growth within the network template pores, when compared to the usually applied potentiostatic or galvanostatic plating conditions.<sup>[47,52]</sup> Under suitable fabrication conditions, the resulting nanowire networks consist of a single, electrochemically grown macroscopic piece of material, made out of up to several billions of interconnected nanowires. All important structural parameters, e.g., wire density, wire diameter and arrangement, can be controlled independently from one another, which is

superior to the other methods mentioned above.<sup>[55]</sup> Chemical composition, purity and crystalline structure of the material are controlled by the parameters employed during the chosen synthesis process.

Here, we present the synthesis of large area 3D Bi NWNWs by electrodeposition in ion track-etched membranes with highly interconnected channels. In addition, measurements of the electrical resistance and cross-plane Seebeck coefficient of 3D NWNW as a function of temperature are presented, discussing the influence of wire diameter and network morphology on its electrical characteristics.

## 2. Results and Discussion

### 2.1. Optimization of Electroplating Parameters

The homogeneity of the Bi NWNWs electrodeposited within a circular area with a diameter of  $8$  mm, was optimized by studying the influence of the ratio between on- and off-potentials ( $U_{\text{ON}}/U_{\text{OFF}}$ ) on the growth process. The ON-pulse was adjusted to optimize the reduction rate of the ions in solution at the working electrode. The OFF-pulse, was adjusted to avoid an effective dissolution or oxidation of the deposited material, while providing time for the ion concentration in the vicinity of the electrodes to be replenished between consecutive ON-pulses. For all depositions, we fabricated identical templates with channel density  $1.4 \times 10^9$  channels/ $\text{cm}^{-2}$  and channel diameter  $\approx 100$  nm. **Figure 1a)** shows the influence of  $U_{\text{ON}}$  on the recorded current-versus-time curves. The same OFF-potential was applied for all samples,  $U_{\text{OFF}} = -170$  mV versus SCE, while  $U_{\text{ON}}$  was varied as  $-200$  mV (red),  $-220$  mV (orange),  $-240$  mV (green), and  $-260$  mV (blue). As seen in **Figure 1a)**, the magnitude of the average current is larger the more negative the applied on-potential  $U_{\text{ON}}$  is. This trend is expected and in agreement with the cyclic voltammetry data (**Figure S2**, Supporting Information). With increasing average current, the time till cap growth becomes shorter, but also the filling ratio decreases (**Figure S3**, Supporting Information). It is known that higher current densities lead to different growth rates in the various channels, and thus to the generation of partially unfilled channels.<sup>[56]</sup> Pulse plating helps to mitigate some of these effects, and thus we achieved a filling ratio of  $\approx 83\%$  for  $U_{\text{ON}}/U_{\text{OFF}} = -200 \text{ mV}/-170 \text{ mV}$  versus SCE. It is expected that a complete filling of the template is achieved by further decreasing  $U_{\text{ON}}$ . In addition, it is observed that the slope of the average current-versus-time increases with more negative  $U_{\text{ON}}$ , indicating diffusion limitation of the current. As the material is deposited along the channel, the remaining empty channel length decreases, effectively decreasing the diffusion length from the bulk solution to the plating site. **Figure 1c,d)** shows the data collected during the pulse plating of the samples shown in **Figure 1b)**. More detailed information on the plots can be found in **Figure S4** (Supporting Information). In **Figure 1c)**, it can be seen that at  $U_{\text{OFF}} = -170$  mV the corresponding current is close to  $0$  mA and only still slightly negative at the end of the pulse ( $t_{\text{OFF}}$ ). This indicates that at this potential, indeed, the concentration of ions close to the electrode is replenished. To visualize the effect of the OFF-pulse on the electrodeposition process,

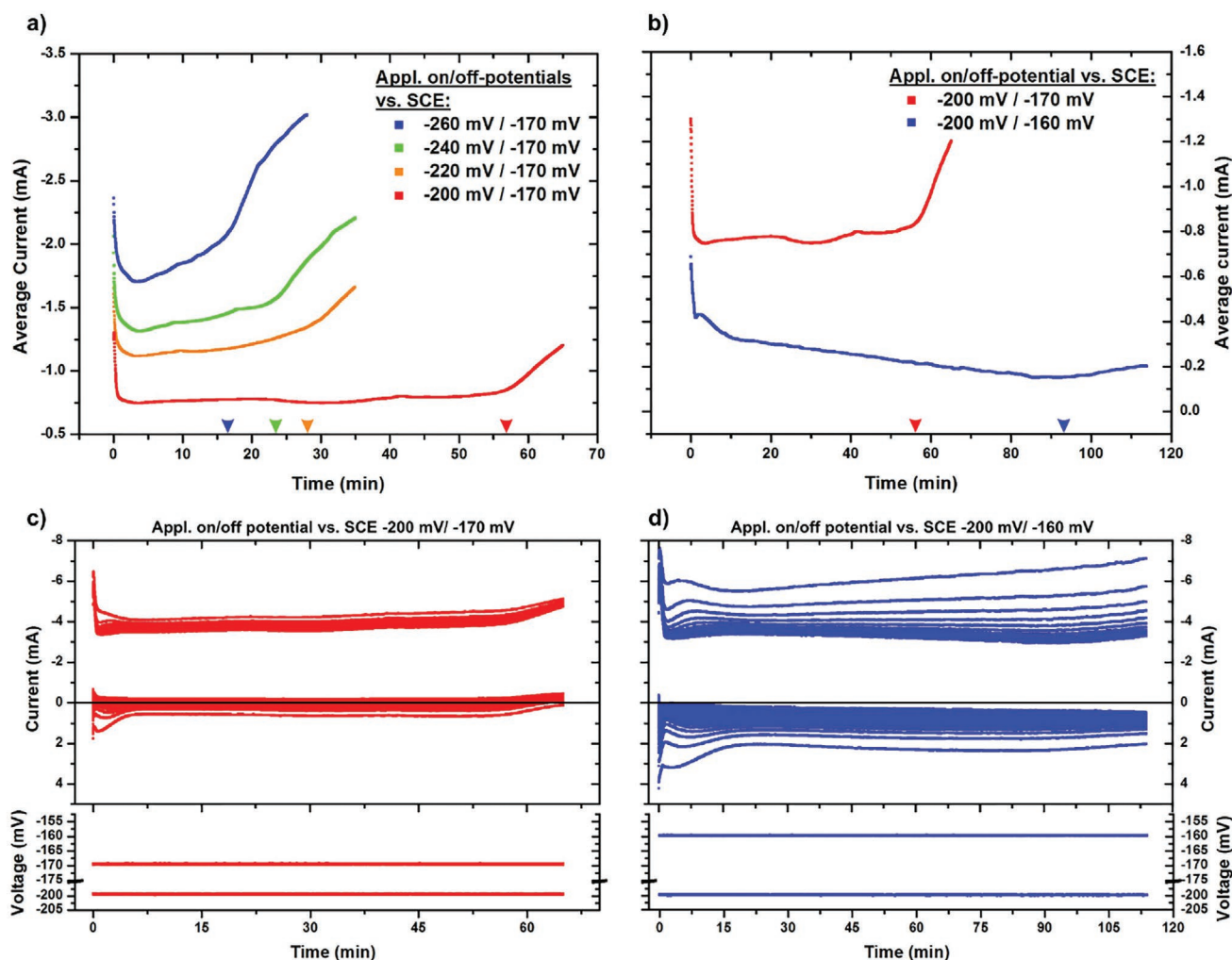


**Figure 1.** a) Average current versus time plots during pulsed electrodeposition at  $U_{\text{OFF}} = -170$  mV, and various  $U_{\text{ON}}$  potentials between  $-200$  mV (red) and  $-260$  mV (blue). The channels in the template had a diameter of  $\approx 100$  nm. b) Average current versus time curves recorded during pulsed electrodeposition with  $U_{\text{ON}}/U_{\text{OFF}}$  being  $-200$  mV/ $-170$  mV (red) and  $-200$  mV/ $-160$  mV (blue). The colored arrows on the time axes in (a,b) mark the respective plating time when cap growth started. c,d) Current- and voltage versus time plots corresponding to the average current versus time plots shown in red and blue, respectively in b). More information on the plots is found in Figure S4 (Supporting Information).

Figure 1b) shows the average current recorded during electrodepositions at  $U_{\text{ON}} = -200$  mV and two different  $U_{\text{OFF}}$  values, namely  $-170$  mV (red) and  $-160$  mV (blue). As discussed above,  $U_{\text{OFF}} = -170$  mV results in a very small negative current, which is optimal to replenish the Bi ion concentration in the vicinity of the working electrode without dissolving or oxidizing the previous plated Bi. By slightly increasing  $U_{\text{OFF}}$  toward less negative potentials, namely  $U_{\text{OFF}} = -160$  mV, the average current decreases significantly (Figure 1b), because  $I_{\text{OFF}}$  is no longer close to zero but positive (Figure 1d), indicating that part of the electrodeposited Bi is being dissolved or oxidized.

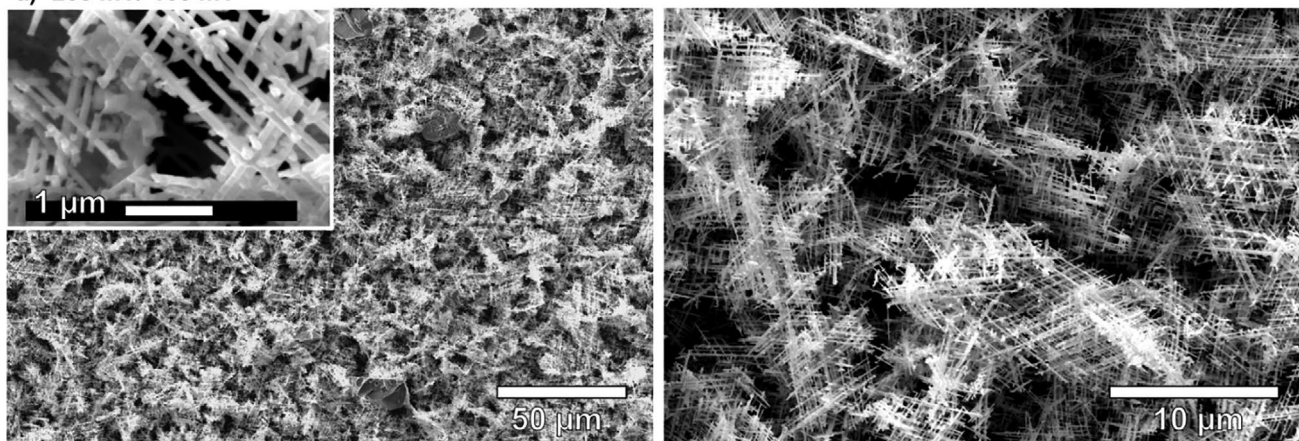
Figure 2 shows SEM images of the Bi NWNWs electrodeposited applying different  $U_{\text{ON}}/U_{\text{OFF}}$ , namely a)  $-200$  mV/ $-160$  mV, b)  $-220$  mV/ $-170$  mV, and c)  $-200$  mV/ $-170$  mV. In all cases, the nanowires exhibit a dense homogeneous appearance. As discussed above, at  $U_{\text{OFF}} = -160$  mV some of the electrodeposited Bi is dissolved again, which results in a rather inhomogeneous nanowire growth and a low filling

ratio of only 40% (Figure 2a). As a consequence, the interconnectivity between adjacent nanowires is incomplete and the network partly disassembled during the dissolution of the polymer template.

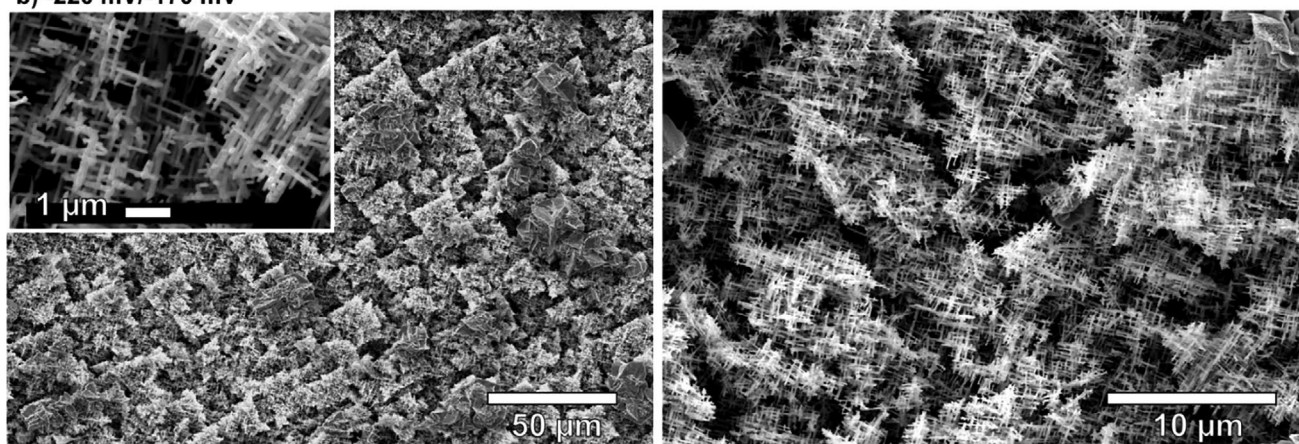
In contrast, the network deposited at  $U_{\text{ON}}/U_{\text{OFF}} = -220$  mV/ $-170$  mV, where Bi is not dissolved during the  $U_{\text{OFF}}$  phase, consists of larger sections of self-supporting nanowire networks. Interestingly, the surface of the network is partitioned into rectangular shaped superstructures. The origin of these superstructures is not yet entirely clarified. However, we assume that they are related to the fourfold spatial orientation of the nanochannels. This assumption is supported by the observation that the superstructures have a triangular shape if the template was irradiated only under three directions, i.e., the membrane exhibits a threefold spatial orientation of the nanochannels (Figure S5, Supporting Information). The number and size of the superstructures is affected by the growth parameters. During the pulse plating either new nuclei are generated



a) -200 mV/-160 mV



b) -220 mV/-170 mV



c) -200 mV/-170 mV

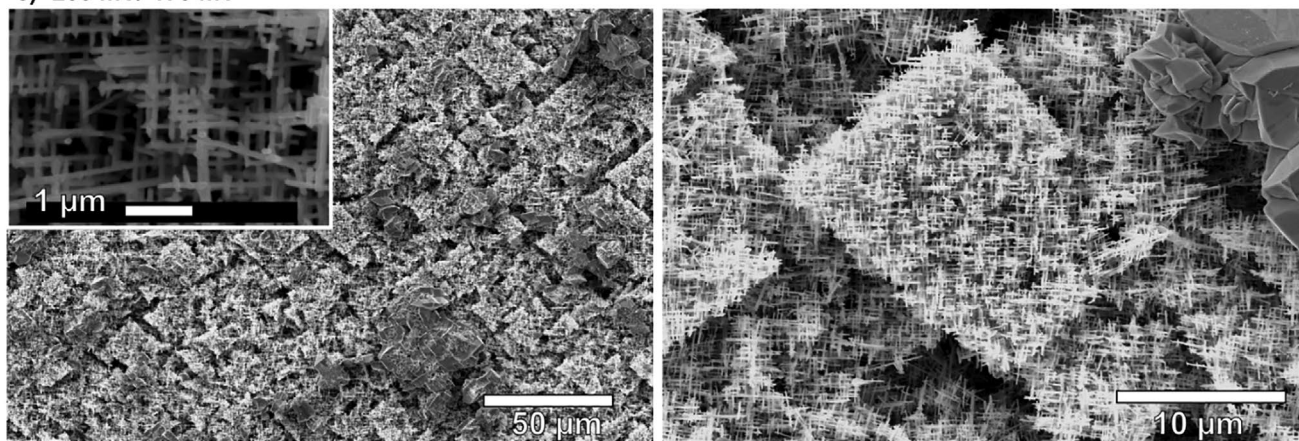


**Figure 2.** SEM images of Bi NWNWs electrodeposited under different  $U_{ON}/U_{OFF}$  potentials,  $t_{ON}$  and  $t_{OFF}$  being 20 and 100 ms, respectively.

or old ones continue to grow. Thus, the formation of the superstructures is closely related to the growth process of material within the channels. Due to the interconnected nature of the channels, the growing nanowire can continue outward in the four directions of the interconnected adjacent channels until merging with neighboring structures. Therefore, the larger

structures result from nuclei that already grew for longer times, while the smaller ones result from younger nuclei.

The filling ratio for this network was  $\approx 66\%$ . Finally, for the NWNW grown at  $U_{ON}/U_{OFF} = -200 \text{ mV}/-170 \text{ mV}$  (Figure 2c), the filling ratio is  $\approx 83\%$  (Figure S3, Supporting Information), and the sample exhibits the most homogeneous growth among



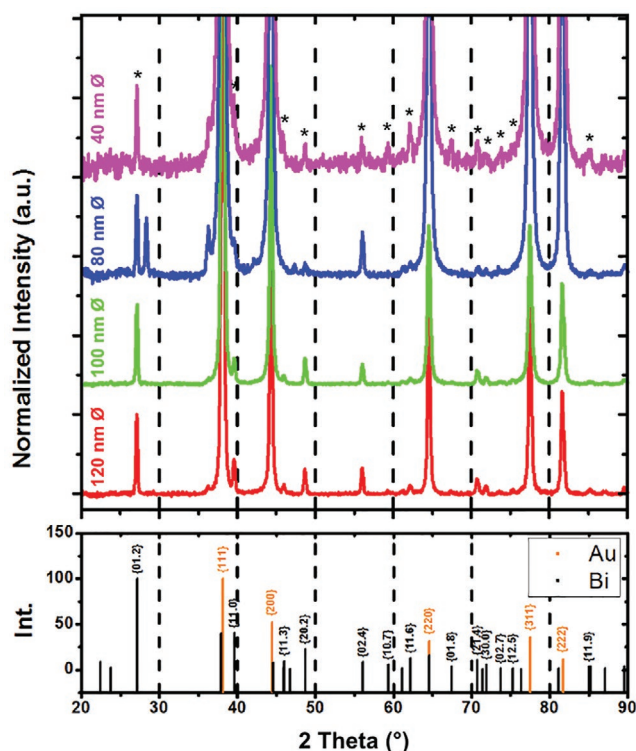


**Figure 3.** Normalized X-ray diffractograms of Bi NWNWs with different wire diameters, deposited with  $U_{ON}/U_{OFF} = -200$  mV/ $-170$  mV versus SCE, at  $40$  °C. The reflexes assigned to Bi are indicated by a star icon for the  $40$  nm diameter sample. At the bottom, the reference data according to JCPDS 5–519 and 4–784 for powder Bi and Au, respectively, are shown.

all tested parameters. Thus, these electrodeposition conditions were applied for the synthesis of Bi NWNWs with tailored geometrical parameters. Their structural and electrical characterization is presented and discussed below.

## 2.2. Crystallographic Characterization

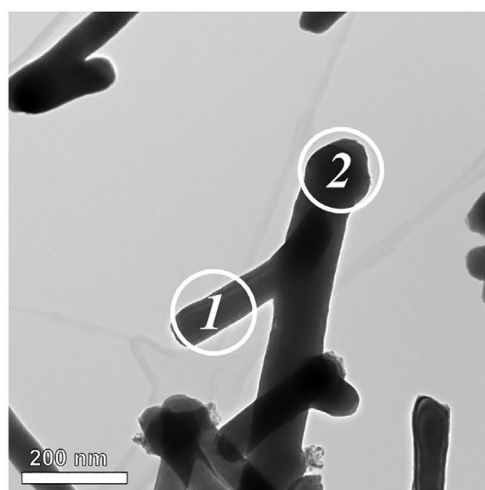
Bi NWNWs with nanowire diameters between  $40$  and  $120$  nm were analyzed by XRD. The growth curves of these different samples are shown in Figure S6 (Supporting Information). Figure 3 shows the corresponding x-ray diffractograms normalized to the  $(01.2)$  reflection. At the bottom, the vertical lines indicate the positions and intensities of the reflections corresponding to powder samples of Bi (JCPDS 5–519) and Au (JCPDS 4–784). The bismuth reference uses a hexagonal lattice. As  $i = -(h+k)$  the index  $i$  is replaced with a dot (.). Unfortunately, some reflections from Bi planes overlap with Au reflections from the Au back electrode, which could not be removed without severely damaging the sample. Reflections that can clearly be assigned to Bi are marked by a black star on the diffractogram of the  $40$  nm diameter networks. Since the channels are inclined by  $45^\circ$  with respect to the membrane surface, the XRD patterns yields reflections by lattice planes that are under  $45^\circ$  with respect to the wire axis. Since the nanowires are also oriented in four different directions with respect

to the membrane normal, the XRD pattern contains many Bi reflections, resembling the pattern of a polycrystalline sample. The normalized reflections exhibit similar intensities for all samples, thus no significant influence of the nanowire diameter on the sample texture could be determined. An additional reflection for all samples can be observed at  $\approx 36.2^\circ$ , close to the Au  $\{111\}$  reflection. This is attributed to tungsten contamination on the Cu anode, which generates a W-L line in addition to the Cu- $K\alpha$  line. For the  $80$  nm sample, there is also an additional reflection at  $\approx 28^\circ$ , which can be assigned to  $\text{Bi}_2\text{O}_3$ . TEM measurements on a single wire intersection of a broken network with a wire diameter of  $80$  nm are shown in Figure 4. The wire fragments are single crystalline over the full length of the inspected segments (few  $100$  nm). The crystal orientation in front of and behind the intersection are identical, indicating that the orientation of the crystal has not been disturbed when the growth reached the intersection. In other cases, changes in crystal orientation across the intersection were also observed (Figure S7, Supporting Information). The TEM investigations revealed a  $(10.1)$  orientation of the nanowire, i.e., the  $c$  axis is oriented with a given angle to the nanowire axis. As comparison, since the transport properties of Bi are highly anisotropic, the highest Seebeck coefficient is expected for Bi nanowires for which the  $c$ -axis (hexagonal description) is parallel to the nanowire axis. To our knowledge, only Bi nanowires synthesized by the on-off technique did exhibit this optimal texture.<sup>[35]</sup>

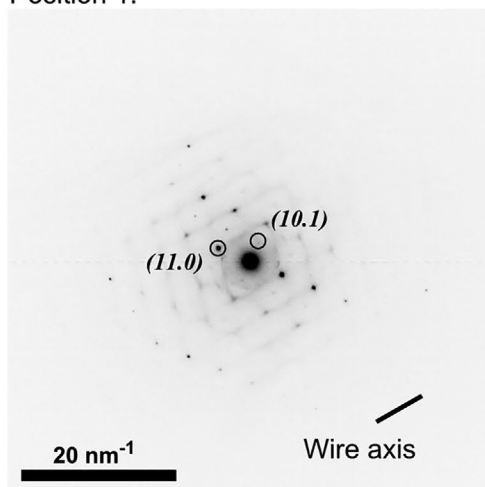
## 2.3. Seebeck Coefficient

Figure 5a shows the Seebeck coefficients of Bi NWNWs as a function of temperature for various wire diameters. The uncertainty is determined based on the assumption that the temperature of the large copper blocks is homogeneous, and that the thermal interface resistance between copper and sample is minimized thanks to the presence of the thermal paste. Contributions to the Seebeck coefficient by the phosphor bronze wires are also neglected as they have a very low Seebeck coefficient over the whole measurement range ( $\approx -0.4$  to  $0$   $\mu\text{V K}^{-1}$ ).<sup>[57]</sup> The largest contribution to the error of the Seebeck coefficient originates from the temperature measurements with the calibrated diodes. At room temperature the Seebeck coefficient decreases with decreasing wire diameter from  $-43.7$   $\mu\text{V K}^{-1}$  ( $140$  nm diameter) to  $-22.8$   $\mu\text{V K}^{-1}$  ( $40$  nm diameter). The values at room temperature are lower than the maximum values reported for bulk Bi but fit well considering the preferred crystal orientation of the wires.<sup>[35,51]</sup> With decreasing temperature, the absolute value of the Seebeck coefficient almost monotonically decreases, changes sign from negative to positive, and with exception of the  $140$  nm diameter sample, reaches a plateau, and decreases again toward zero (Figure 5a).

At  $55$  K the Seebeck coefficients of all samples measured are positive. The transition temperature at which the sign change occurs decreases with increasing wire diameter (Figure 5b). Assuming a linear relation between wire diameter and transition temperature, the sign change should not occur any longer for samples with a wire diameter of about  $210$  nm and larger. At  $300$  K the Seebeck coefficient decreases almost linearly with decreasing wire diameter, whereas at  $60$  K the values of the



Position 1:



Position 2:

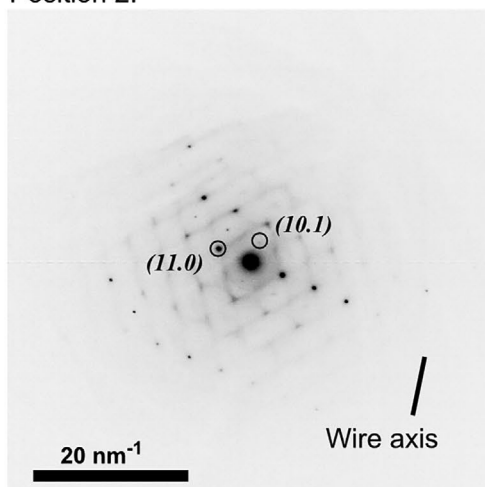


**Figure 4.** TEM image and SAED patterns of broken Bi nanowire network segments with wires of  $\approx 80$  nm diameter. The crystal structure in front of and behind the intersection is the same.

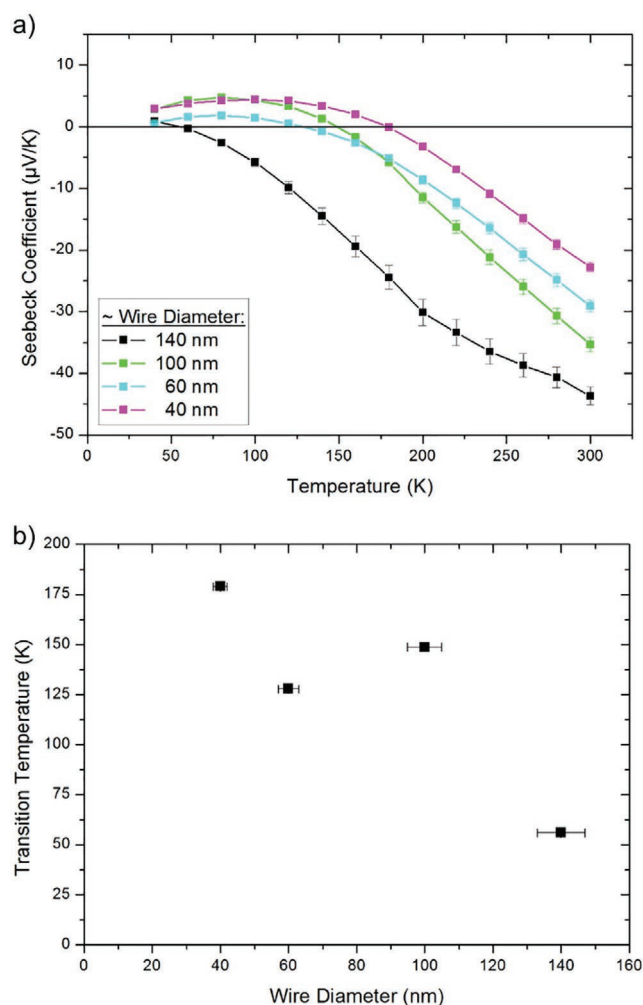


**Figure 5.** a) Seebeck coefficients of Bi NWNWS measured between 300 and 40 K. Lines serve as guide to the eye. b) Transition temperature where Seebeck coefficient changes sign as a function of wire diameter.

different wires fluctuate around a few  $\mu\text{V K}^{-1}$  without a clear trend.

A similar dependence between Seebeck coefficient of nanowires and nanowire diameter was theoretically predicted by Murata et al.<sup>[51]</sup> The group modelled the carrier transport behavior in Bi nanowires, taken into account limitations in the mean free path of the charge carriers in low-dimensional systems. For Bi crystals oriented along the bisectrix orientation, a sign change is predicted when the mobility of the holes becomes larger than that of the electrons.

In our experiments, the change of the Seebeck coefficient sign stops to occur at wire diameters smaller than those predicted by Murata et al. This can be due to various reasons, including geometrical and morphological effects due to the network structure, the crystal orientation of the deposited wires not being exactly along the bisectrix axis, defects in the wire structure, or unequal densities of electron and hole charge carriers. In turn, the theoretical predictions did not take into account the presence of surface states, which may play a role

due to the large surface to volume ratio of the nanowires.<sup>[22,40,49]</sup> In addition, the crystalline structure of wires with different diameters may vary and as such also contribute to the discrepancy between theoretical prediction and experiment. Usually wires with smaller diameter exhibit a stronger texture along the wire axis.<sup>[50,58,59]</sup> Finally, the defect density might also change as a function of wire diameter.

## 2.4. Electrical Resistance

The electrical properties of Bi nanostructures are extremely interesting. Given the semimetallic character of Bi and the associated small carrier concentration, the resistance of bulk Bi decreases with lowering temperature due to the dominant decrease in carrier mobility. However, Bi nanowires synthesized by different techniques have mostly exhibited a non-monotonic resistance versus temperature behavior, which is diameter and crystallinity dependent.<sup>[35,49,51,60,65]</sup> The non-monotonicity results from the complex interplay between charge carrier density and carrier mobility, which are a function of temperature, crystal size and nanowire diameter. This non-monotonic behavior has been described also using classical size effects based on the models of Fuchs, Mayadas and Dingle, considering the scattering of charge carriers at the surface and at grain boundaries.<sup>[24–28,61]</sup> In the case of nanowire arrays and networks, due to the high density of contacted nanowires, the electrical resistance values of the networks are very small ( $\approx \mu\text{ohm}$ ), significantly smaller than the resistances of cables and/or contacts ( $\approx \text{mohm}$ ). In addition, since the exact number of connected wires is unknown, only relative values with respect to the resistance at 280 K can be provided.<sup>[35,49,51,60,65]</sup>

Figure 6 shows the electrical resistance of bismuth NWNWs as a function of temperature. For the networks with smallest nanowire diameter (40 nm), the resistance decreases with decreasing temperature, indicating the influence of surface states. Kim et al. reported also a similar behavior for  $\approx 40$  nm diameter Bi wires grown by the ON-OFF method.<sup>[35]</sup> The better-known non-monotonic  $R$  versus  $T$  behavior, previously reported for parallel Bi nanowire arrays, is observed for the networks with 60 and 100 nm diameter wires. Finally, the resistance of the network with 140 nm diameter wires, i.e., densest, exhibits a monotonic increase with decreasing temperature. It has been previously reported, that in the case of a non-monotonic  $R$  versus  $T$  behavior, the resistance maximum shifts to lower temperatures for wires consisting of smaller grains.<sup>[15]</sup> Thus, for Bi nanowires consisting of sufficiently small crystals the resistance becomes a monotonic function of temperature, as reported by Liu et al.<sup>[65]</sup> Thus, since the individual wires in the network are polycrystalline and the network structure has a large density of interconnections, the sample exhibits a monotonical resistance increase with decreasing temperature. From studies on parallel Bi nanowire arrays, it is known, that the grain size decreases with increasing nanowire diameter.<sup>[15]</sup> These results indicate that by tailoring crystallinity and interconnectivity of the 3D nanowire assemblies, their electrical properties can be adjusted. In the future, the influence of the interconnections will be systematically studied, also in comparison to arrays

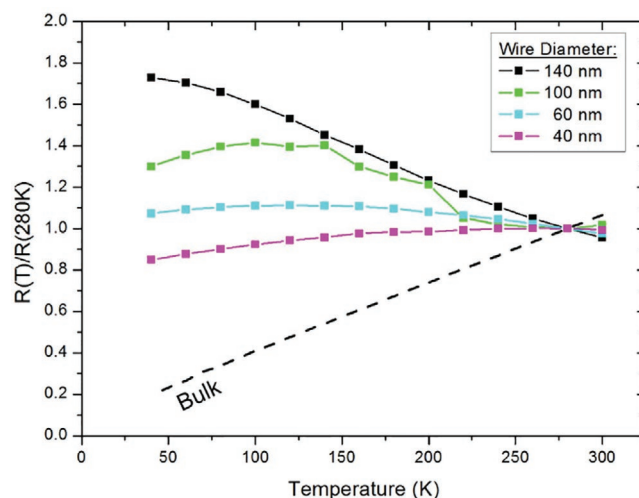


**Figure 6.** Temperature dependence of the electrical resistance of Bi NWNW normalized by the resistance at 280 K. Lines serve as guide to the eyes. The values for bulk resistance are extracted from.<sup>[35]</sup>

of parallel wires with same diameter and crystallographic properties.

## 3. Conclusion

By pulsed electroplating in combination with etched ion-track templates, 3D Bi NWNWs were fabricated with excellent control on wire diameter, wire density and alignment. The applied pulse potentials were optimized to maximize the filling ratio. After release from the template, the resulting networks are shown to be highly interconnected and mechanically self-supporting. XRD measurements with  $45^\circ$  angle to the wire axis indicate a polycrystalline growth of the network. As the alignment of the wires within the network may obscure the measurement no conclusion about a possible texture can currently be drawn. TEM measurements on small network fragments suggest single crystallinity of wire sections of at least a few 100 nm.

Seebeck coefficient and relative electrical resistance of Bi NWNWs embedded in polycarbonate membranes were measured systematically between 300 and 40 K. With decreasing temperature, all samples displayed a sign change from a negative to a positive Seebeck coefficient. The smaller the wire diameter, the higher the transition temperature. This behaviour is attributed to the mean free path limitation of the charge carriers for small wire diameters and is in good agreement with previous theoretical predictions by Murata et al. For wire diameters smaller than 140 nm, the observed size effect in the Seebeck coefficient is also explained by limitations of the mean free path as well as by contributions of surface states to the transport properties. Size effects also contribute to the diameter-dependent non-monotonic behavior of the electrical resistance of bismuth NWNWs as a function of temperature. The size-dependent Seebeck coefficient opens the road to the production of all-Bi thermocouples with legs made from nanowires with different diameters.

## 4. Experimental Section

### 4.1. Template Fabrication

Polycarbonate foils (Makrofol N, Bayer AG, thickness 30  $\mu\text{m}$ ), were irradiated at the UNiversal Linear ACcelerator (UNILAC) of the GSI Helmholtz Center for Heavy Ion Research in Darmstadt (Germany) using Au ions of  $\approx 2.2$  GeV kinetic energy. At this energy, the range of the ions is much larger than the thickness of the PC samples. The foils were irradiated in four consecutive steps under  $45^\circ$  beam incidence, rotating the foil each time by  $90^\circ$  around its axis (Figure S8, Supporting Information). For each direction, the ion beam had a fluence of  $5 \times 10^8$  ions  $\text{cm}^{-2}$ . As the sample is tilted toward the incoming beam, the fluence on the sample surface is equal to the fluence multiplied by the cosine of the tilt angle. Summing up all four irradiations, this leads to a total fluence of  $1.4 \times 10^9$  ions  $\text{cm}^{-2}$ . Along its trajectory, each ion generates a highly localized cylindrical damage zone of a few nanometers in diameter.

Prior to etching, the irradiated foils were exposed to UV light (T-30M Vilber Lourmat lamp, 30 W, 312 nm) for 2 h. UV exposure yields a narrower pore-size distribution of the channels in the membranes.<sup>[62]</sup>

To convert the ion tracks into open channels, the irradiated foils were immersed in a 6 M NaOH solution (NaOH pellets by Carl Roth purity  $\geq 98\%$ ) at  $50^\circ\text{C}$ .<sup>[55]</sup> Different etching times were applied to obtain templates with 30 nm up to 400 nm channel diameter. The etching process is stopped by immersing the foils in distilled deionized water (Millipore Direct-Q5). A cross section of an etched template can be found in Figure S9 in the Supporting Information.

Once the foils were dried, a  $\approx 200$  nm Au layer was sputtered on one side of the template (Edwards Sputter Coater S150B). This layer was reinforced with a  $\approx 1$   $\mu\text{m}$  thick electroplated Au layer by using a commercial electrolyte (Gold-SF, Metakem GmbH), a GAMRY Reference 600 potentiostat, and applying  $U = -0.7$  V versus an Au spiral at room temperature. This additional layer guaranteed a good mechanical stability of the Au layer as well as the complete closure of the pores so that any leakage of the electrolyte through the pores is prevented.

### 4.2. Nanowire Synthesis

Electrodeposition of Bi inside the channels was carried out using an aqueous electrolyte consisting of 0.1 mol  $\text{L}^{-1}$  Bi(III)-chloride (Merck, for analysis), 0.3 mol  $\text{L}^{-1}$  tartaric acid (Carl Roth, 99.5%), 0.2 mol  $\text{L}^{-1}$  NaCl (Merck, for analysis), 1.95 mol  $\text{L}^{-1}$  HCl (Carl Roth, 99.5%), and 1.09 mol  $\text{L}^{-1}$  glycerol (Carl Roth, 99.5%).<sup>[46,47]</sup> A small amount of surfactant, 1 mL  $\text{L}^{-1}$  DOWFAX 2A1, was added to the electrolyte to improve the wettability of the PC template.<sup>[8,48]</sup>

Electroplating was done at  $40^\circ\text{C}$ . In order to ensure the complete wetting of the interconnected channels, the sample was immersed into the electrolyte 2 h before plating, while the setup was heating up. For electroplating a three-electrode setup consisting of a  $\text{Pt}_{80}\text{Ir}_{20}$  spiral as counter electrode, a standard calomel electrode (sat. KCl) (SCE) (Sensortechnik Meinsberg) as reference electrode, and the Au back-electrode as working

electrode was used. Pulse plating was applied to achieve a more homogeneous Bi growth inside the pores over the whole plating area.<sup>[47–49,63]</sup> During the on-potential ( $U_{\text{ON}}$ ), the Bi ions get reduced while during the off-potential ( $U_{\text{OFF}}$ ) the ions redistribute in the vicinity of the electrode and the diffusion layer thickness shrinks.

Five individual voltage pulses and the corresponding recorded current are shown in Figure 7a. These pulses were recorded at the 20 min mark in Figure 7b. Figure 7b shows the recorded data of all pulses during a plating. The continuous lines appear because individual ms short pulses merge on a 70 min total time axis. Figure 7c displays the average current of 10 consecutive pulses versus plating time. This data presentation allows to identify the different regimes during the process.<sup>[48,49]</sup> As in the case of potentiostatic deposition, the average current during pulse deposition remains almost constant throughout the growth of the nanowires in the channels. The current then increases once the channels are filled and caps start to grow on top.<sup>[48,49]</sup> The complete filling of the channels and the start of cap growth are defined by the time of intersection of two tangents adjacent to the currents before and after the current increase (marked by orange dashed lines in Figure 7c).

Prior to electrical characterization, it is very important to estimate the filling ratio achieved during deposition. The filling ratio is defined as  $\text{FR} = Q_{\text{exp}} \cdot Q_{\text{theo}}^{-1}$ , with  $Q_{\text{theo}}$  being the charge required to fill all the pores.  $Q_{\text{theo}}$  is estimated by the Faraday law,  $Q_{\text{theo}} = m \cdot z \cdot F \cdot (\eta \cdot M)^{-1}$ , with  $m = \rho \cdot V$  being the mass required to completely fill all channels,  $\rho = 9.78$  g  $\text{cm}^{-3}$  being the density of bismuth,  $z = 3$  being the valence number of Bi,  $F$  the Faraday constant,  $\eta$  the current efficiency, and  $M$  the molar mass. Assuming a current efficiency  $\eta$  of 100%, the charge  $Q_{\text{exp}}$  is given by the integrated charge that was deposited until the moment when caps start to grow.

The crystallographic properties of the NWNWs were studied using a Seifert, XRD 3003 PTS-3 in Bragg–Brentano geometry. For these measurements, the nanowires remained embedded in the polymer membrane. To index the reflexes, powder reference data JCPDS 4–784 (Au) and JCPDS 5–519 (Bi) were used. The wire morphology was investigated using a JEOL JSM-7401F HRSEM scanning electron microscope after removal of the polycarbonate membrane in several baths of dichloromethane (DCM, Merck, for analysis). For individual nanowires, selected area electron diffraction patterns were recorded using a JEOL JEM-ARM200F high resolution transmission electron microscope (HRTEM). In this case, the wires were transferred onto Cu-lacey TEM grids (Plano GmbH) by drop-casting after applying an ultrasonic bath to detach the nanowires from the backelectrode.

### 4.3. Setup for Seebeck Coefficient and Electrical Measurements

The Seebeck coefficient and the electrical resistance of the samples were measured using a custom-built setup described in.<sup>[8,40,48,63]</sup> A schematic of the setup is shown in Figure 8. For these measurements, the nanowire network remained embedded in the polymer membrane and was placed between two copper blocks. A gold layer (thickness  $\approx 400$  nm) was



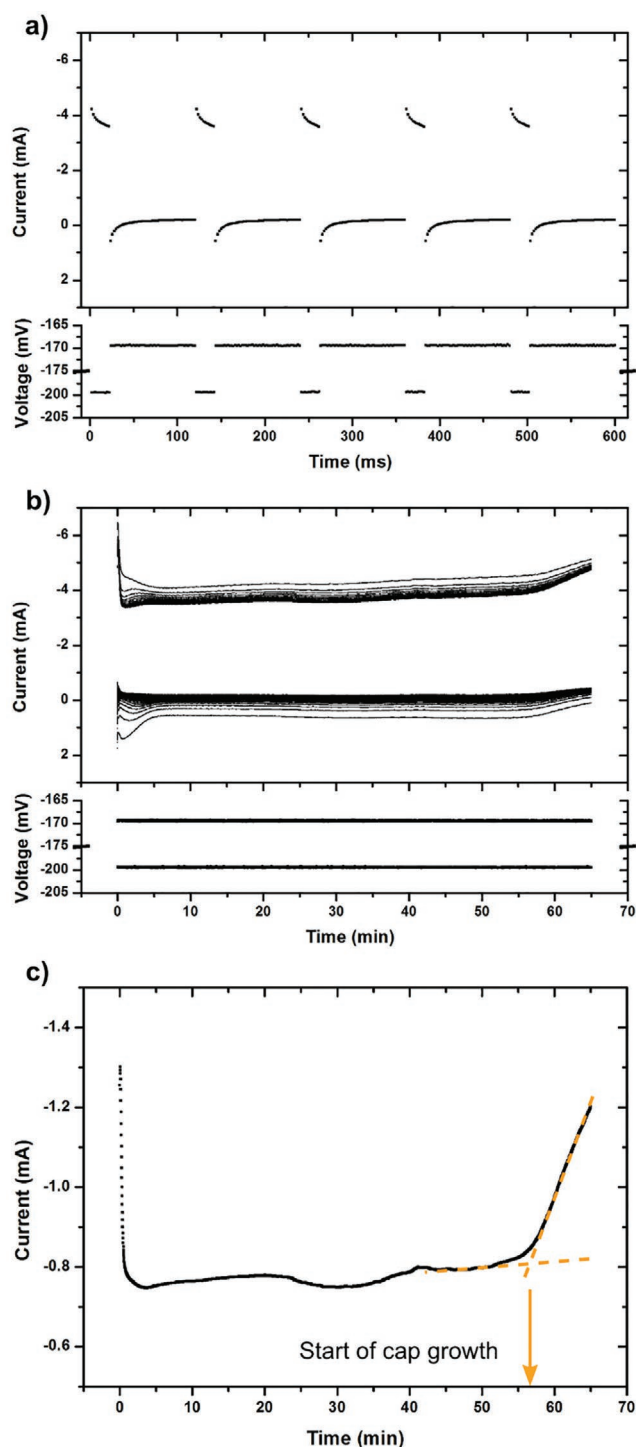


**Figure 7.** Current response during five consecutive voltage pulses. The pulses were recorded at the 20 min mark in Figure 1b). b) Current versus time curves recorded during plating of a Bi nanowire network using voltage pulses of ms width, shown in Figure 1a). The appearing lines in (b) are an artefact explained in Figure S4 in the Supporting Information. c) Average current (each 10 consecutive pulses) versus plating time.<sup>[48]</sup> When the current steeply increases, the channels are filled and caps start to grow on top of the template surface (indicated by arrow).

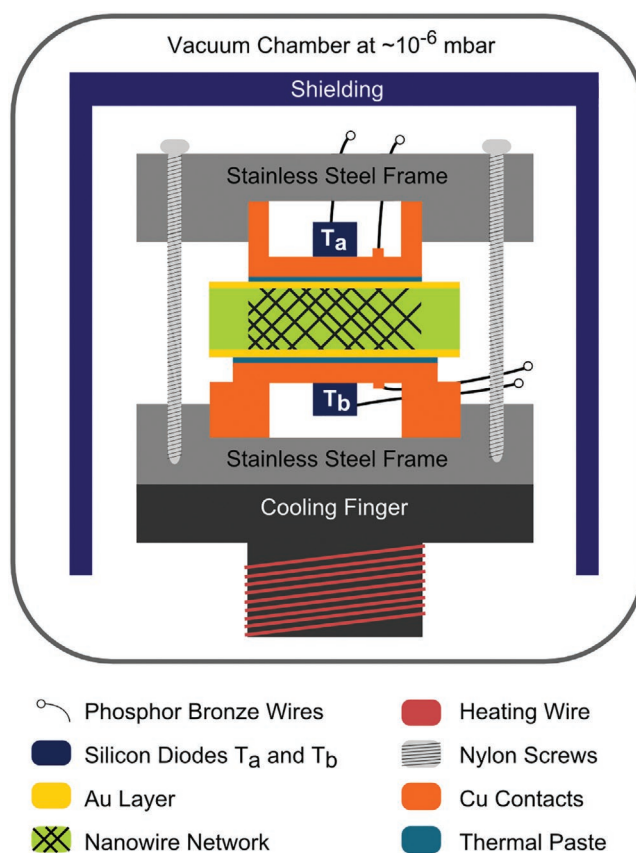


**Figure 8.** Custom-built setup for the characterization of the cross-plane Seebeck coefficient and electrical resistance.

sputtered on the cap side in order to guarantee a good electrical contact between the nanowire network and the upper copper block. The Au back-electrode served as a contact to the lower copper block. The copper blocks are connected to four point probes for electrical measurement and to two diodes for temperature control. In order to determine the Seebeck coefficient, a dynamic temperature difference was generated by heating and cooling the sample from below. As the heat transfer to the top Cu block via the nanowire sample is relatively slow, its temperature cannot achieve equilibrium with the bottom Cu block, generating the temperature difference.<sup>[8]</sup> The recorded thermovoltage exhibited the expected linear dependency as a function of the temperature difference between top and bottom. The slope of the curve provides the Seebeck coefficient of the samples at ambient temperature. The Seebeck coefficient and electrical resistance measurements were performed at various temperatures between 300 and 40 K in steps of 20 K. The sample chamber was kept at a pressure of  $\sim 10^{-6}$  mbar to avoid heat loss via convection. Every 10 s the following values were recorded: temperature of the two diodes, thermovoltage, and  $I$ - $U$  characteristic. The latter provided the electrical resistance of the embedded NWNWs. For each sample, two sets of experiments were carried out: i) For the electrical resistance measurements, the polymer with the embedded NWNW and the conductive layers on the front and back was squeezed between the two Cu blocks, as described above. ii) To deduce

the Seebeck coefficient, an additional thin layer of thermal paste (PK-1 Thermal Compound by ProLimatech) was applied between the sample and the copper blocks in order to reduce the thermal resistance and thus minimize the uncertainty of the deduced Seebeck coefficient.<sup>[40]</sup>

## Supporting Information

Supporting Information is available from the Wiley Online Library or from the author.

## Acknowledgements

The authors gratefully acknowledge financial support by the Deutsche Forschungsgemeinschaft (DFG) within the priority programs SPP 1386 and SPP 1666. M.F.P.W. thanks the Helmholtz School for Hadron and Ion Research "HGS-HIRE" and the RheinMain University of Applied Sciences for financial support. The nanowire samples were produced based on UMAT irradiations performed at the beam line X0 at the GSI Helmholtzzentrum für Schwerionenforschung, Darmstadt (Germany) in the frame of FAIR Phase-0.

Open access funding enabled and organized by Projekt DEAL.

## Conflict of Interest

The authors declare no conflict of interest.

## Data Availability Statement

Research data are not shared.

## Keywords

bismuth, electrodeposition, ion tracks, nanowires, thermoelectrics, thin films

Received: November 2, 2020

Revised: December 21, 2020

Published online: January 27, 2021

- [1] M. Rauber, I. Alber, S. Müller, R. Neumann, O. Picht, C. Roth A. Schokel, M. E. Toimil-Molares, W. Ensinger, *Nano Lett.* **2011**, *11*, 2304.
- [2] J. Martin, M. Martin-Gonzalez, J. F. Fernandez, O. CaballeroCalero, *Nat. Commun.* **2014**, *5*, 5130.
- [3] L. Movsesyan, A. W. Maijenburg, N. Goethals, W. Sigle, A. Spende, F. Yang, B. Kaiser, W. Jaegermann, S.-Y. Park, G. Mul, C. Trautmann, M. E. Toimil-Molares, *Nanomaterials* **2018**, *8*, 693.
- [4] G. Pennelli, M. Totaro, M. Piatto, P. Bruschi, *Nano Lett.* **2013**, *13*, 2592.
- [5] L. Movsesyan, I. Schubert, L. Yeranyan, C. Trautmann, M. E. Toimil-Molares, *Semicond. Sci. Technol.* **2016**, *31*, 014006.
- [6] M. Lindeberg, H. Yousef, H. Rödjegård, H. Martin, K. Hjort, *J. Micromech. Microeng.* **2008**, *18*, 065021.
- [7] A. Hashim, in *Nanowires – Implementations and Applications*, Intech, London **2011**, Ch. 14.
- [8] M. F. P. Wagner, F. Völklein, H. Reith, C. Trautmann, M. E. Toimil-Molares, *Phys. Status Solidi A* **2016**, *213*, 610.
- [9] M. T. W. Wang, A. Abdulagatov, S. M. George, Y.-C. Lee, R. Yang, *Nano Lett.* **2012**, *12*, 655.
- [10] I. Paulowicz, V. Hrkac, S. Kaps, V. Cretu, O. Lupan, T. Braniste, V. Duppel, I. Tiginyanu, L. Kienle, R. Adelung, Y. K. Mishra, *Adv. Electron. Mater.* **2015**, *1*, 1500081.
- [11] A. Ponzoni, E. Comini, G. Sberveglieri, *Appl. Phys. Lett.* **2006**, *88*, 203101.
- [12] A. Ruiz-Clavijo, S. Ruiz-Gomez, O. Caballero-Calero, L. Perez, M. Martin-Gonzalez, *Phys. Status Solidi RRL* **2019**, *13*, 1900263.
- [13] J. Heremans, *Acta Phys. Pol. A* **2005**, *108*, 609.
- [14] T. Cornelius, M. E. Toimil-Molares, *Nanowires* (Ed: P. Prete), Intech, Croatia **2010**, p. 414.
- [15] T. W. Cornelius, M. E. Toimil-Molares, R. Neumann, S. Karim, *J. Appl. Phys.* **2006**, *100*, 114307.
- [16] T. W. Cornelius, M. E. Toimil-Molares, R. Neumann, G. Fahsold, R. Lovricic, A. Pucci, S. Karim, *Appl. Phys. Lett.* **2006**, *88*, 103114.
- [17] T. W. Cornelius, M. E. Toimil-Molares, S. Karim, R. Neumann, *Phys. Rev. B* **2008**, *77*, 125425.
- [18] S. B. Cronin, Y.-M. Lin, O. Rabin, M. R. Black, J. Y. Ying, M. S. Dresselhaus, P. L. Gai, J.-P. Minet, J.-P. Issi, *Nanotechnology* **2002**, *13*, 653.
- [19] M. R. Black, M. Padi, S. B. Cronin, Y.-M. Lin, O. Rabin, T. McClure, G. Dresselhaus, P. L. Hagelstein, M. S. Dresselhaus, *Appl. Phys. Lett.* **2000**, *77*, 4142.
- [20] M. R. Black, Y.-M. Lin, S. B. Cronin, O. Rabin, M. S. Dresselhaus, *Phys. Rev. B* **2002**, *65*, 195417.
- [21] J. Cornett, O. Rabin, *Appl. Phys. Lett.* **2011**, *98*, 182104.
- [22] J. Gooth, J. G. Glusckke, R. Zierold, M. Leijnse, H. Linke, K. Nielsch, *Semicond. Sci. Technol.* **2014**, *30*, 015015.
- [23] A. I. Hochbaum, R. Chen, R. D. Delgado, W. Liang, E. C. Garnett, M. Najarian, A. Majumdar, P. Yang, *Nature* **2008**, *451*, 163.
- [24] K. Fuchs, *Math. Proc. Cambridge Philos. Soc.* **1938**, *34*, 100.
- [25] A. Mayadas, M. Shatzkes, *Phys. Rev. B* **1970**, *1*, 1382.
- [26] K. Fuchs, *Math. Proc. Cambridge Philos. Soc.* **1936**, *34*, 100.
- [27] R. B. Dingle, *Proc. R. Soc. A* **1950**, *201*, 545.
- [28] E. Sondheimer, *Adv. Phys.* **2001**, *50*, 499.
- [29] J. Heremans, C. Trush, *Phys. Rev. B* **1999**, *59*, 12579.
- [30] L. Hicks, M. Dresselhaus, *Phys. Rev. B* **1993**, *47*, 12727.
- [31] O. Roslyak, A. Piryatinski, *J. Appl. Phys.* **2016**, *119*, 125107.
- [32] M. Verdier, D. Lacroix, K. Termentzidis, *Phys. Rev. B* **2018**, *98*, 155434.
- [33] T. E. Huber, M. J. Graf, *Phys. Rev. B* **1999**, *60*, 16880.
- [34] K. J. Norris, J. Zhang, D. M. Fryauf, A. Rugar, A. Flores, T. J. Longson, A. J. Lohn, N. P. Kobayashi, *Proc. SPIE* **2012**, *8467*, 84670E.
- [35] J. Kim, W. Shim, W. Lee, *J. Mater. Chem. C* **2015**, *3*, 11999.
- [36] F. Y. Yang, K. Liu, K. Hong, D. H. Reich, P. C. Searson, C. L. Chien, *Science* **1999**, *21*, 5418.
- [37] M. E. Toimil-Molares, N. Chtanko, T. W. Cornelius, D. Dobrev, I. Enculescu, R. H. Blick, R. Neumann, *Nanotechnology* **2004**, *15*, S201.
- [38] Y.-M. Lin, S. B. Cronin, J. Y. Ying, M. S. Dresselhaus, J. P. Heremans, *Appl. Phys. Lett.* **2000**, *76*, 3944.
- [39] Y.-M. Lin, X. Sun, M. S. Dresselhaus, *Phys. Rev. B* **2000**, *62*, 4610.
- [40] M. Cassinelli, S. Müller, K.-O. Voss, C. Trautmann, F. Völklein, J. Gooth, K. Nielsch, M. E. Toimil-Molares, *Nanoscale* **2017**, *9*, 3169.
- [41] T. W. Cornelius, J. Brötz, N. Chtanko, D. Dobrev, G. Miehle, R. Neumann, M. E. Toimil-Molares, *Nanotechnology* **2005**, *16*, S246.
- [42] C. Tang, G. H. Li, X. C. Dou, Y. X. Zhang, L. Li, *J. Phys. Chem. C* **2009**, *113*, 5422.
- [43] Y.-T. Cheng, A. M. Weiner, C. A. Wong, M. P. Balogh, M. J. Lukitsch, *Appl. Phys. Lett.* **2002**, *81*, 3248.
- [44] J. Reppert, R. Rao, M. Skove, J. He, M. Craps, T. Tritt, A. M. Raob, *Chem. Phys. Lett.* **2007**, *442*, 334.
- [45] D. Glocker, M. Skove, *Phys. Rev. B* **1977**, *15*, 608.

- [46] S. Müller, C. Schötz, O. Picht, W. Sigle, P. Kopold, M. Rauber, I. Alber, R. Neumann, M. E. Toimil-Molares, *Am. Chem. Soc.* **2012**, 12, 615.
- [47] M. Cassinelli, S. Müller, Z. Aabdin, N. Peranio, O. Eibl, C. Trautmann, M. E. Toimil-Molares, *Nucl. Instrum. Methods Phys. Res., Sect. B* **2015**, 365, 668.
- [48] M. F. P. Wagner, *Ph.D. Thesis*, Technische Universität Darmstadt **2018**.
- [49] M. Cassinelli, *Ph.D. Thesis*, Technische Universität Darmstadt **2016**.
- [50] O. Picht, S. Müller, I. Alber, M. Rauber, J. Lensch-Falk, D. L. Medlin, R. Neumann, M. E. Toimil-Molares, *J. Phys. Chem. C* **2012**, 116, 5367.
- [51] M. Murata, A. Yamamoto, Y. Hasegawa, T. Kornine, A. Endo, *J. Appl. Phys.* **2017**, 121, 014303.
- [52] A. Ruiz-Clavijo, O. Caballero-Calero, M. Martín-González, *Nanomaterials* **2018**, 8, 345.
- [53] C. Trautmann, *Nucl. Instrum. Methods Phys. Res., Sect. B* **1995**, 105, 81.
- [54] O. Eibel, K. Nielsch, N. Peranio, F. Völklein, in *Thermoelectric Bi<sub>2</sub>Te<sub>3</sub> Nanomaterials*, Wiley-VCH, Weinheim **2015**, p. 34.
- [55] M. E. Toimil-Molares, *Beilstein J. Nanotechnol.* **2012**, 3, 860.
- [56] K. S. Napolskii, I. V. Roslyakov, A. A. Eliseev, D. I. Petukhov, A. V. Lukashin, S.-F. Chen, C.-P. Liu, G. A. Tsirlina, *Electrochim. Acta* **2011**, 56, 2378.
- [57] E. Mun, S. L. Bud'ko, M. S. Torikachvili, P. C. Canfield, *Meas. Sci. Technol.* **2010**, 21, 055104.
- [58] S. Karim, M. E. Toimil-Molares, F. Maurer, G. Miehe, W. Ensinger, J. Liu, T. W. Cornelius, R. Neumann, *Appl. Phys. A* **2006**, 84, 403.
- [59] J. Liu, J. L. Duan, M. E. Toimil-Molares, S. Karim, T. W. Cornelius, D. Dobrev, H. J. Yao, Y. M. Sun, M. D. Hou, D. Mo, Z. G. Wang, R. Neumann, *Nanotechnology* **2006**, 17, 1922.
- [60] Z. Zhang, X. Sun, M. S. Dresselhaus, J. Y. Ying, J. Heremans, *Phys. Rev. B* **2000**, 61, 4851.
- [61] F. Völklein, E. Kessler, *Phys. Status Solidi B* **1986**, 134, 351.
- [62] E. Ferain, R. Legras, *Nucl. Instrum. Methods Phys. Res., Sect. B* **1993**, 82, 539.
- [63] S. Müller, *Ph.D. Thesis*, Ruprecht-Karls-Universität Heidelberg **2012**.
- [64] J. Heremans, C. M. Thrush, Y.-M. Lin, S. Cronin, Z. Zhang, M. S. Dresselhaus, J. F. Mansfield, *Phys. Rev. B* **2000**, 61, 2921.
- [65] K. Liu, C. L. Chien, P. C. Searson, K. Yu-Shang, *Appl. Phys. Lett.* **1998**, 73, 1436.